nature energy

Article

https://doi.org/10.1038/s41560-023-01443-0

Single-phase local-high-concentration solid polymer electrolytes for lithium-metal batteries

Received: 30 January 2023

Accepted: 14 December 2023

Published online: 12 January 2024

Check for updates

Weiran Zhang[1], Volodymyr Koverga[2,3], Sufu Liu[4], Jigang Zhou[5], Jian Wang[5], Panxing Bai[4], Sha Tan[6], Naveen K. Dandu[2,3], Zeyi Wang[4], Fu Chen[7], Jiale Xia[4], Hongli Wan[4], Xiyue Zhang[4], Haochen Yang[4], Brett L. Lucht[8], Ai-Min Li[4], Xiao-Qing Yang[6], Enyuan Hu[6], Srinivasa R. Raghavan[4] ✉, Anh T. Ngo[2,3] ✉ & Chunsheng Wang[1,4] ✉

Solid polymers are promising electrolytes for Li-metal batteries, but they have limitations: they cannot simultaneously achieve high ionic conductivity, good mechanical strength and compatibility with high-voltage cathodes while suppressing Li dendrites. Here, we design a class of locally high-concentration solid polymer electrolytes based on polymer blends, which are termed Li-polymer in F diluter (LPIFD). The Li-polymer (polymer-in-salt) ensures continuous Li-ion conduction channels and contributes to the solid electrolyte interphase (SEI), and the F diluter (inert fluorinated polymer) adds mechanical strength. Studies reveal that a single-phase LPIFD, which is based on a miscible polymer blend, lacks phase boundaries and forms an organic-less and LiF-rich SEI, effectively suppressing lithium dendrites. The single-phase LPIFD delivers ionic conductivity of 3.0×10^{-4} S cm^{-1}, and enables the Li anode to reach a high coulombic efficiency of 99.1% and a critical current density of 3.7 mA cm^{-2}. Furthermore, the ability to form an F-rich cathode electrolyte interphase allows $LiNi_{0.8}Co_{0.1}Mn_{0.1}O_2$||Li cells to achieve a cycle life of 450 cycles at a high operating voltage of 4.5 V. This design will inspire efforts to commercialize polymer electrolytes for high-energy Li-metal batteries.

Lithium (Li) metal batteries are recognized as the next generation of energy storage devices due to their high energy density and safety[1,2]. However, the growth of Li dendrites on Li anodes and the instability of high-voltage cathodes remain unresolved challenges and limit their commercialization[3–6]. Since most electrolytes are not stable against Li-metal anodes, a solid electrolyte interphase (SEI) on the Li anode is formed[7–9]. However, the SEI is not robust enough to suppress lithium dendrites[10,11], which reduces the Li plating/stripping coulombic efficiency (CE) and the cycle life of the cell.

Studies with liquid electrolytes have demonstrated that inorganic-rich (especially LiF-rich) SEIs can suppress Li dendrites. This is because LiF is highly lithiophobic (that is, it has a weak affinity

[1]Department of Materials Science and Engineering, University of Maryland, College Park, MD, USA. [2]Materials Science Division, Argonne National Laboratory, Lemont, IL, USA. [3]Department of Chemical Engineering, University of Illinois Chicago, Chicago, IL, USA. [4]Department of Chemical and Biomolecular Engineering, University of Maryland, College Park, MD, USA. [5]Canadian Light Source Inc., University of Saskatchewan, Saskatoon, Saskatchewan, Canada. [6]Chemistry Division, Brookhaven National Laboratory, Upton, NY, USA. [7]Department of Chemistry and Biochemistry, University of Maryland, College Park, MD, USA. [8]Department of Chemistry, University of Rhode Island, Kingston, RI, USA. ✉e-mail: sraghava@umd.edu; anhngo@uic.edu; cswang@umd.edu

https://doi.org/10.1038/s41560-023-01443-0

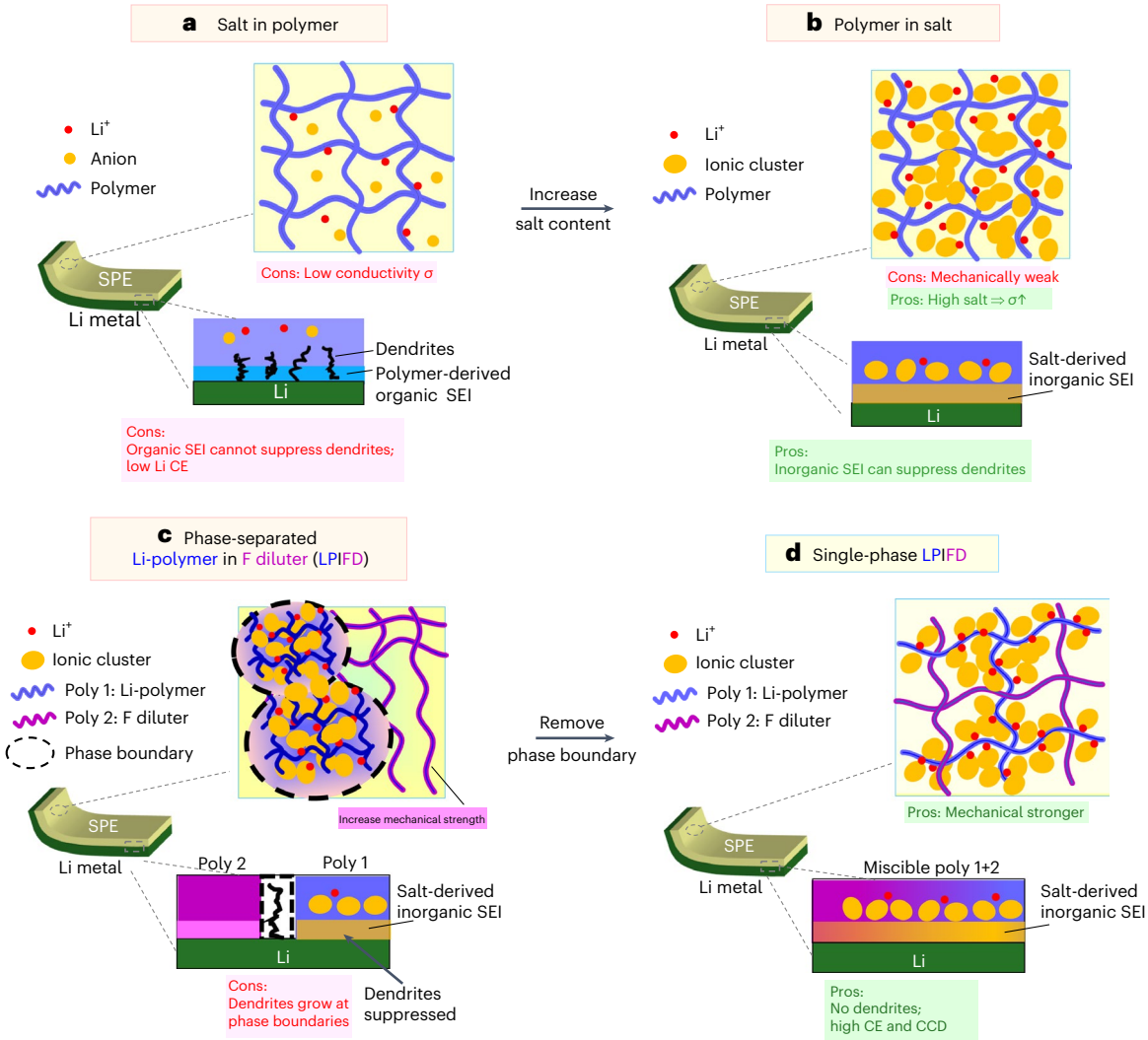

Fig. 1 | Schematic of the logic for designing single-phase LPIFD SPEs. a, Salt-in-polymer electrolyte. **b**, Polymer-in-salt electrolyte. **c**, Phase-separated LPIFD. **d**, Single-phase LPIFD. Poly, polymer.

to Li). Therefore, Li migrates along the Li/SEI interface but Li dendrites do not grow through a LiF SEI (refs. 12–14). In addition, LiF cathode electrolyte interphases (CEIs) have a high anodic stability of >6.0 V, which enables the use of high-voltage cathodes[15,16]. In liquid electrolytes, the reduction of fluorinated inorganic anions (such as PF_6^- and bis(fluorosulfonyl)imide (FSI^-)) produces an inorganic lithiophobic LiF-rich SEI, whereas the reduction of organic solvents forms an organic/inorganic lithophilic SEI. To promote anion reduction and suppress solvent reduction, researchers have explored the use of high-concentration electrolytes[17–19]. To reduce the electrolyte viscosity while maintaining the same SEI composition, high-concentration electrolytes have been dissolved in fluorinated diluents to form localized high-concentration electrolytes[20–22]. On a different note, solid ceramic electrolytes have high mechanical strength and form inorganic SEIs, which should be ideal for Li-metal batteries[23,24]. However, the critical current density (CCD) of solid ceramic electrolytes is still limited, partly due to the inability to form LiF SEIs from the reduction of solid ceramic electrolytes. Additionally, the existence of grain boundaries promotes Li-dendrite growth[25–27].

Solid polymer electrolytes (SPEs) can potentially combine the merits of liquid electrolytes (formation of LiF SEI and low interfacial resistance) and solid ceramic electrolytes (high mechanical strength). However, high CE values are rarely reported for SPEs in Li-metal batteries[28,29], and most Li-metal cells with SPEs have a low areal capacity[30] due to the low CCD. This is because the organic-rich SEIs formed in SPEs cannot suppress the growth of lithium dendrites (Fig. 1a). To form LiF-rich SEIs, a fluoroethylene carbonate (FEC) liquid solvent has been added to SPEs. However, the reduction of FEC also generates substantial organic composition in SEIs. Therefore, the Li CE reaches only 97.6% with a CCD of 3.2 mA cm^{-2}, which is still limited[20,31,32]. Like high-concentration electrolytes, high-concentration polymer electrolytes (polymer-in-salt based on polyacrylonitrile or polyethylene oxide (PEO)) have also been reported to form LiF-rich SEIs[33,34]. The high salt concentration and the solvent residues absorbed by the salt enhance the ionic conductivity. However, these also result in poor mechanical strength, thereby limiting their application in Li-metal batteries (Fig. 1b). Researchers have attempted to enhance the mechanical strength of these electrolytes by adding an inert support matrix[35–38] or using block copolymers[39]. For instance, Zhao et al. incorporated a combination of poly(ethylene carbonate) and poly(vinylidene fluoride-co-hexafluoropropylene) (PVDF-HFP) with a concentrated salt localized to the poly(ethylene carbonate) (ref. 40). However, these systems are typically phase-separated and inhomogeneous, which is unfavourable for achieving uniform Li deposition and SEI formation. Notably, Li dendrites can still grow along the phase boundaries[40–43] (Fig. 1c).

Herein, we demonstrate a new electrolyte based on a polymer blend, which we term Li-polymer in F diluter (LPIFD). The single-phase LPIFD is a locally high-concentration polymer electrolyte formed by combining two miscible polymers: Li-polymer (polymer-in-salt) and F diluter (inert fluorinated polymer) (Fig. 1d). The F diluter, which is inert for Li-ion conduction, imparts high mechanical strength. Moreover, the Li-polymer, along with a high salt content, provides high Li-ion conduction and contributes to the formation of a LiF-rich SEI, effectively suppressing Li-dendrite growth. Crucially, the high miscibility of the Li-polymer with the F diluter eliminates phase boundaries, further enhancing the ability to suppress Li dendrites. As a result, the single-phase LPIFD exhibits both high mechanical strength and good Li-dendrite suppression.

As a concept demonstration, a fluorine-rich PVDF-HFP was selected as the inert F diluter. PVDF and its corresponding polymer blends have been widely investigated for polymer electrolytes[44], but there is a notable gap in guidance for their design to attain high performance with an Li anode. To illustrate the influences of phase boundary and SEI on the performance of LPIFD, we studied a series of polymers for the Li-polymers: poly(propylene carbonate) (PPC), PEO, poly(methyl methacrylate) (PMMA), poly(vinylsulfonyl fluoride) (PVSF) and poly(bis(trifluoroethoxy)phosphazene) (PTFEP). The salt was lithium bis(fluorosulfonyl)imide (LiFSI). Among these Li-polymers, PPC and PEO are not miscible with PVDF-HFP, resulting in phase-separated LPIFD[45,46] (Fig. 1c). PMMA is miscible with PVDF-HFP (ref. 47), but the reduction of an ester group gives rise to an organic-rich SEI, which reduces Li CE and dendrite suppression ability. The fluorination of polymers (PVSF and PTFEP) enhances their compatibility with the F diluter[48]. Moreover, fluorination increases the F content and weakens the interaction with Li^+, thus promoting the formation of inorganic-rich fluorinated SEI. Consequently, the single-phase LPIFD electrolytes with inorganic-rich fluorinated SEI exhibit strong Li-dendrite suppression, as indicated by a high Li plating/stripping CE of 99.1% and a CCD of 3.7 mA cm^{-2}. In addition, the single-phase LPIFD electrolyte forms an F-rich CEI with a high-voltage stability to 5.4 V. This would allow batteries to cycle at a cutoff voltage >4.5 V, which is yet to be demonstrated[49]. Consequently, our electrolytes enable Li||$LiNi_{0.8}Co_{0.1}Mn_{0.1}O_2$ (NMC811) cells to reach a CE of 99.95% for 450 cycles at a cutoff voltage of 4.5 V and a CE of 99.91% for over 200 cycles even at a cutoff voltage of 4.6 V. The exceptional performance of these cells is attributed to (1) excellent Li-dendrite suppression due to the formation of organic-less and LiF-rich SEI and the lack of phase boundaries along with uniform Li deposition; (2) high-voltage stability due to the formation of a F-rich CEI; and (3) enhanced ionic conductivity (3.0×10^{-4} S cm^{-1}) and mechanical strength. Additionally, the LPIFD concept for designing polymer electrolytes is versatile and can be applied as an interlayer or binder for ceramic solid-state electrolytes and also for micro-silicon anodes.

Design of LPIFD electrolytes

We selected PVDF-HFP as the F diluter because it has excellent mechanical properties and relatively high stability with lithium metal and high-voltage cathodes[50–53]. We selected inorganic LiFSI as the salt because it is reduced to form a LiF-rich inorganic SEI on Li metal without organic by-products, unlike LiTFSI. The high content of LiFSI facilitates the formation of aggregated interconnective ionic clusters, thus promoting the formation of LiF SEI and providing percolation pathways for ion migration[33,54]. For the Li-polymer, we wanted a polymer that was miscible with the F diluter, so that their mixture would form a single-phase LPIFD. We also wanted the polymer to have the capability to form LiF-rich SEI. With these considerations in mind, we investigated five polymers (Fig. 2).

The first two polymers, PPC and PEO, are non-miscible with PVDF-HFP, which forms phase-separated LPIFD. Of these two, PEO demonstrates greater stability with lithium metal compared to PPC-LPIFD because the decomposition of polycarbonate could result in a high

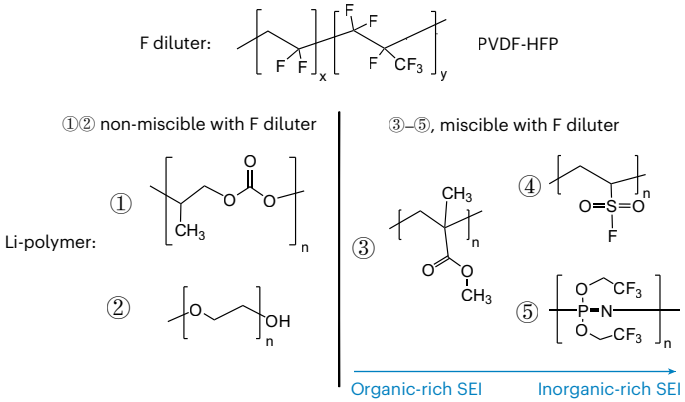

Fig. 2 | Design of LPIFD electrolytes. LPIFD electrolytes are composed of F diluter (PVDF-HFP) and an Li-polymer (LiFSI with (1) PPC, (2) PEO, (3) PMMA, (4) PVSF or (5) PTFEP).

amount of organic composition in SEI while polyethers are relatively stable at low potential. However, the phase separation notably weakens the Li-dendrite suppression. Of the three polymers that are miscible with PVDF-HFP, PMMA was found to form an organic-rich SEI, which is not desirable. PVSF is an upgraded version of PMMA. Even though the S=O on PVSF has a strong interaction with Li, which tends to be reduced, the almost inorganic nature promotes the formation of an organic-less SEI with the LiF in it (reduction of S–F). Meantime, PTFEP is enriched with inorganic elements, and its weaker interaction with Li promotes the reduction of anion, allowing for an organic-less and LiF-rich SEI. To underscore the importance of developing a single-phase structure and an inorganic-rich fluorinated SEI, we choose three representative LPIFDs, namely those based on PEO, PMMA and PTFEP, for a detailed structural and property characterization. To comprehensively illustrate the electrolyte design principle, the electrochemical performance of five LPIFD electrolytes was also compared.

The composition of the LPIFD was first optimized. To check the miscibility of PTFEP and PVDF-HFP, their blends were investigated by scanning electron microscopy (SEM), energy-dispersive X-ray spectroscopy (Supplementary Figs. 1–3) and differential scanning calorimetry (Supplementary Fig. 4). PTFEP is semi-crystalline[55] but has considerable backbone flexibility[56,57] and the strong electron-withdrawing ability of the trifluoromethyl group implies a weaker interaction of PTFEP with Li^+ (ref. 58), which is promising for ionic conduction. At a PTFEP/PVDF-HFP weight ratio of 0.4, a homogeneous structure with continuous ionic conduction channels was formed, as can be seen from the uniform morphology obtained from SEM and energy-dispersive X-ray spectroscopy and from the single glass-transition temperature (T_g) from differential scanning calorimetry (Supplementary Note 1). LiFSI was then added into the above polymer blend (Supplementary Note 2) until the salt content reached 63 wt%. The resulting electrolyte (denoted as PTFEP-LPIFD) has a low T_g of −63 °C (Supplementary Fig. 4c) and a high ionic conductivity 3.0×10^{-4} S cm^{-1} at room temperature with a low activation energy E_a = 0.18 eV (Supplementary Fig. 5). The high ionic conductivity is attributed to the high concentration of salt and the solvent absorbed by the salt.

For comparison, we prepared PMMA-LPIFD and PEO-LPIFD with the same composition ratio as the PTFEP-LPIFD. The precursor solutions of the three LPIFDs and images of the membranes are shown in Supplementary Figs. 6 and 7. The solvent residues remaining in the electrolytes were estimated with nuclear magnetic resonance (NMR) spectroscopy (Supplementary Fig. 8). We found that 16–19 wt% 1,2-dimethoxyethane (DME) was present in all cases. These remaining solvents served as a high-concentration plasticizer strongly bound with Li^+ ions that are localized against inert PVDF-HFP (ref. 59). Although the solvent residue and high salt content can potentially weaken the

mechanical properties of polymer electrolytes, all three LPIFDs still had a strong solid-like rheology (Supplementary Fig. 9, with their storage modulus G' » their loss modulus G'') (Supplementary Note 3). Among the three, PEO-LPIFD shows phase separation (Supplementary Fig. 10), with S elements (LiFSI) present more in the O-rich domain (PEO-rich) (Supplementary Fig. 11), consistent with the immiscibility of PEO and PVDF-HFP. In contrast, PMMA-LPIFD and PTFEP-LPIFD exhibit a flat and uniform surface (Supplementary Figs. 12 and 14) and uniform element mapping (Supplementary Figs. 13 and 15), as expected from the miscibility of the polymers. Moreover, the single-phase LPIFDs were very dense and lacking the distinct porous structure often observed in PVDF-based polymer electrolytes[44].

Structure and properties of LPIFD electrolytes

To understand the structure and chemistry of PEO-, PMMA- and PTFEP-LPIFD polymer electrolytes, a selected membrane region from each was characterized by scanning transmission X-ray microscopy (STXM) at the C, O and F K-edges (Fig. 3). The different colours in Fig. 3a–c represent different regions on the LPIFD electrolytes and their corresponding absorption information (Fig. 3d–f). The spectra for PEO-LPIFD show the immiscibility between PEO and the PVDF-HFP. Note the distinct spectra in the green and red regions (Fig. 3a,d and Supplementary Fig. 16a,d). The red region is PEO-rich. In the C-edge spectra, the peak at 289.3 eV corresponds to the C–O bonds in PEO (ref. 60). The green region is rich in PVDF-HFP, and the peak at 292.3 eV corresponds to the C–F resonance in PVDF-HFP (ref. 61). In sharp contrast, both the PMMA- and PTFEP-LPIFD spectra show the miscibility of their constituent polymers (Fig. 3b,e and Supplementary Fig. 16b,e for PMMA and Fig. 3c,f and Supplementary Fig. 16c,f for PTFEP). Molecular dynamics simulations were conducted to complement the STXM observations at the atomistic level. The snapshots and the density profiles again confirm the poor miscibility of PEO with PVDF-HFP and a predominance of LiFSI in the PEO-rich region (Fig. 3g). In contrast, both PMMA and PTFEP are largely miscible with PVDF-HFP (Fig. 3h–i). This could be a result of the difference in the polarity of the polymers (Supplementary Fig. 17).

The STXM at the N and F K-edges (Supplementary Figs. 18 and 19) also reveal information about the extent of Li–FSI aggregation: this is higher in the PTFEP-LPIFD electrolyte than in the PEO- and PMMA-LPIFD electrolytes (Supplementary Note 4). This is attributed to the weaker interaction of PTFEP with Li^+ due to the electron-withdrawing $-CF_3$ group on the side chain, which has been quantitatively confirmed (Supplementary Fig. 20). Indeed, Li^+ is prone to interact with more polar monomer fragments with highly negatively charged atomic sites, particularly –O– of PEO, O= and –O– of PMMA, and =N– and –O– in PTFEP. The coordination ability of Li···(O=)FSI calculated from the Li^+ local environment indicates strong Li–FSI interionic interactions inherent to LPIFDs (Supplementary Fig. 21)[22,62–64]. The high coordination ability of FSI and a high probability of Li–FSI aggregates (Supplementary Figs. 22 and 23) in LPIFD is attributed to the high concentration of Li salt and the presence of the fluorinated diluter.

The coordination environment of three LPIFD samples was characterized using oxygen K-edge X-ray absorption spectroscopy (XAS) before and after mixing with LiFSI salt (Fig. 3j). Upon mixing LiFSI salt into PEO/PVDF-HFP blends, the C–O peak at 532.08 eV shifts to higher energy due to the solvation of ethereal oxygen by Li^+ (ref. 65). Similarly, the C=O and C–O peaks in the PMMA/PVDF-HFP blend (at 531.1 and 531.9 eV) also shift to higher energy in the corresponding LPIFD (ref. 66). A similar shift of the O peak at 532.0 eV in the PTFEP/PVDF-HFP blend is also observed in the corresponding LPIFD, suggesting that Li^+ solvation with O also occurs in this system. Moreover, the Fourier transform infrared (FTIR) spectroscopy (Fig. 3k, detailed analysis in Supplementary Note 5) proves the interaction of Li^+ with O and –P=N– in PTFEP. These interactions provide fast channels for Li^+ conduction, resulting in the high ionic conductivity of the LPIFDs. The weak interaction of Li^+ with PVDF-HFP was also confirmed (Fig. 3k).

The relative interaction strengths of Li^+, FSI^- and the polymer could be inferred from the large peaks beyond 535 eV (Fig. 3j), which were ascribed to S=O bonds[67,68]. As this molecular orbital is antibonding in nature, a higher energy level suggests a stronger interaction between Li^+ and FSI^-. This implies that in PTFEP-LPIFD, the interaction between Li^+ and FSI^- is stronger than that of other LPIFDs, while the interaction between Li^+ and the polymer is weaker, promoting the reduction of anion to form an organic-less SEI. In addition, the XAS results of the three LPIFDs before and after mixing with LiFSI salt were also calculated using density functional theory (DFT) (Supplementary Fig. 24). Good agreement with the experimental peaks was found (Supplementary Fig. 25).

In LPIFD electrolytes, the ionic conductivity, transference number and mechanical strength are well correlated with the single-phase structure. In Supplementary Fig. 5, it is observed that PEO-LPIFD exhibits the lowest ionic conductivity and highest activation energy (E_a) among the three LPIFDs because the phase separation between PEO and PVDF-HFP blocks the ion-conductive channels. Conversely, the single-phase structures of PMMA-LPIFD and PTFEP-LPIFD result in higher ionic conductivity. The latter has the highest conductivity, which is probably due to the weaker interaction of Li^+ and the corresponding higher solvent residue in that case. Turning now to the Li-ion transference number (t_{Li^+}), its values are 0.38 for PEO-LPIFD (Supplementary Fig. 26a), 0.53 for PMMA-LPIFD (Supplementary Fig. 26b) and 0.64 for PTFEP-LPIFD (Supplementary Fig. 26c), Again, the higher t_{Li^+} for the latter two is because of their single-phase structure, which ensures that there is a homogeneous distribution of the Li salt. Note that the t_{Li^+} for PTFEP-LPIFD surpasses that of typical SPEs (ref. 69). The high t_{Li^+} facilitates efficient Li^+ transport and also helps to suppress Li dendrites by reducing the concentration gradient[70,71].

Next, regarding the mechanical properties, PEO is immiscible with PVDF-HFP, resulting in mechanically weaker PEO/PVDF-HFP blends compared to PVDF-HFP. In contrast, both PMMA and PTFEP are miscible with PVDF-HFP, enhancing the mechanical properties of PMMA/PVDF-HFP and PTFEP/PVDF-HFP blends over PVDF-HFP (Supplementary Fig. 27). As a result, even with a higher Li salt content, PTFEP-LPIFD is much stronger (modulus 23.3 MPa, Supplementary Fig. 28) and more thermally stable (Supplementary Figs. 29 and 30) than well-known PEO-based SPEs (Supplementary Note 6). This highlights the superiority of the single-phase LPIFD design.

SEI chemistry and Li anode stability with LPIFD electrolytes

The distinctive Li-polymer compositions of the three LPIFDs result in varied SEI chemistry. Figure 4 presents an X-ray photoelectron spectroscopy (XPS) analysis of SEI on Li anodes after cycling for three LPIFDs. As intended, LPIFD promotes the formation of organic-less SEI due to the high LiFSI salt concentration. During the argon sputtering (depth profiling from top to bottom), a notable decrease in the ratio of carbon (organic species) in the SEI of PEO-LPIFD is observed (Fig. 4a). This trend is also evident in the C 1*s* and O 1*s* spectra, for which the C–C peak and Li_2CO_3 peaks decrease (Supplementary Fig. 31a), whereas the Li_2O peak gradually increases (Supplementary Fig. 32a) and the LiF peak remains strong (Supplementary Fig. 33a). In contrast, the SEI formed in PMMA-LPIFD (Fig. 4b, and Supplementary Figs. 31b–34b) exhibits a considerably higher ratio of organic to inorganic components compared to that of PEO-LPIFD. This is attributed to the lower stability of the ester functional group of PMMA with Li metal than polyether, similar to liquid localized high-concentration carbonate electrolytes, for which the solvent decomposition leads to an elevated carbon content in the SEI (refs. 15,72). No C–F is detected in the SEI of PEO-LPIFD and PMMA-LPIFD, whereas C–F is present in the SEI of PTFEP-LPIFD (Supplementary Figs. 31c and 33c), indicating the

https://doi.org/10.1038/s41560-023-01443-0

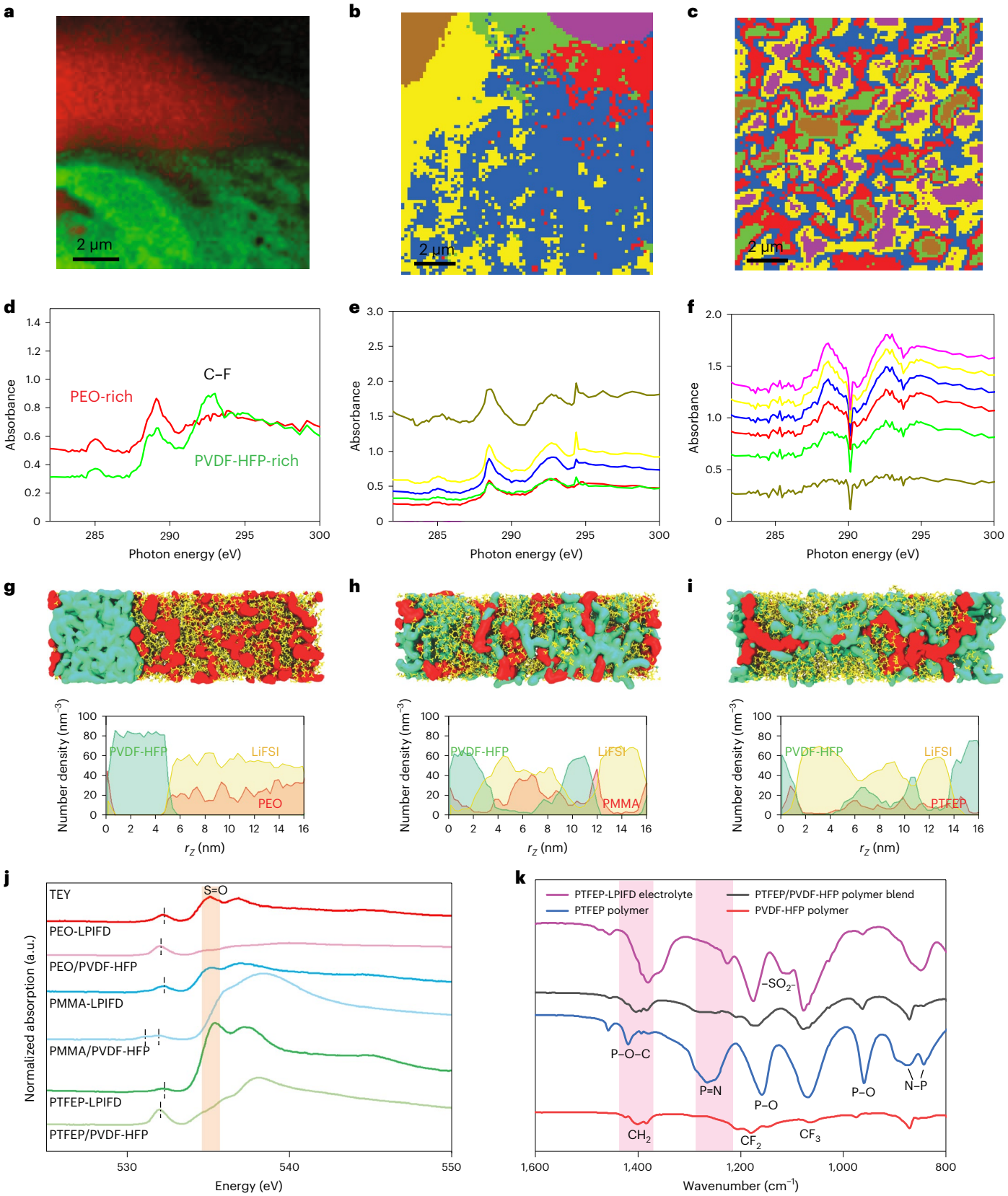

Fig. 3 | Properties of phase-separated and single-phase LPIFD. a–**c**, STXM images of PEO-LPIFD (**a**), PMMA-LPIFD (**b**) and PTFEP-LPIFD (**c**). **d**–**f**, C K-edge XAS spectra of PEO-LPIFD (**d**), PMMA-LPIFD (**e**) and PTFEP-LPIFD (**f**) extracted at various colored regions in STXM images. **g**–**i**, Snapshots of equilibrated structures and density profiles of phase-separated PEO-LPIFD (**g**), single-phase PMMA-LPIFD (**h**) and PTFEP-LPIFD (**i**), as simulated by molecular dynamics. The density profile is plotted in the direction of the normal vector of the *x* axis of the equilibrated cell and represents the concentration distribution of the constituents. Yellow beads stand for FSI. Red indicates PEO/PMMA/PTFEP and green PVDF-HFP. **j**, Oxygen K-edge XAS spectra of PEO/PVDF-HFP polyblends and PEO-LPIFD, PMMA/PVDF-HFP polyblends and PMMA-LPIFD, and PTFEP/PVDF-HFP polyblends and PTFEP-LPIFD. **k**, FTIR spectra of PTFEP, PVDF-HFP, PTFEP/PVDF-HFP blends, and PTFEP-LPIFD polymer electrolytes. a.u., arbitrary units; TEY, total electron yield.

https://doi.org/10.1038/s41560-023-01443-0

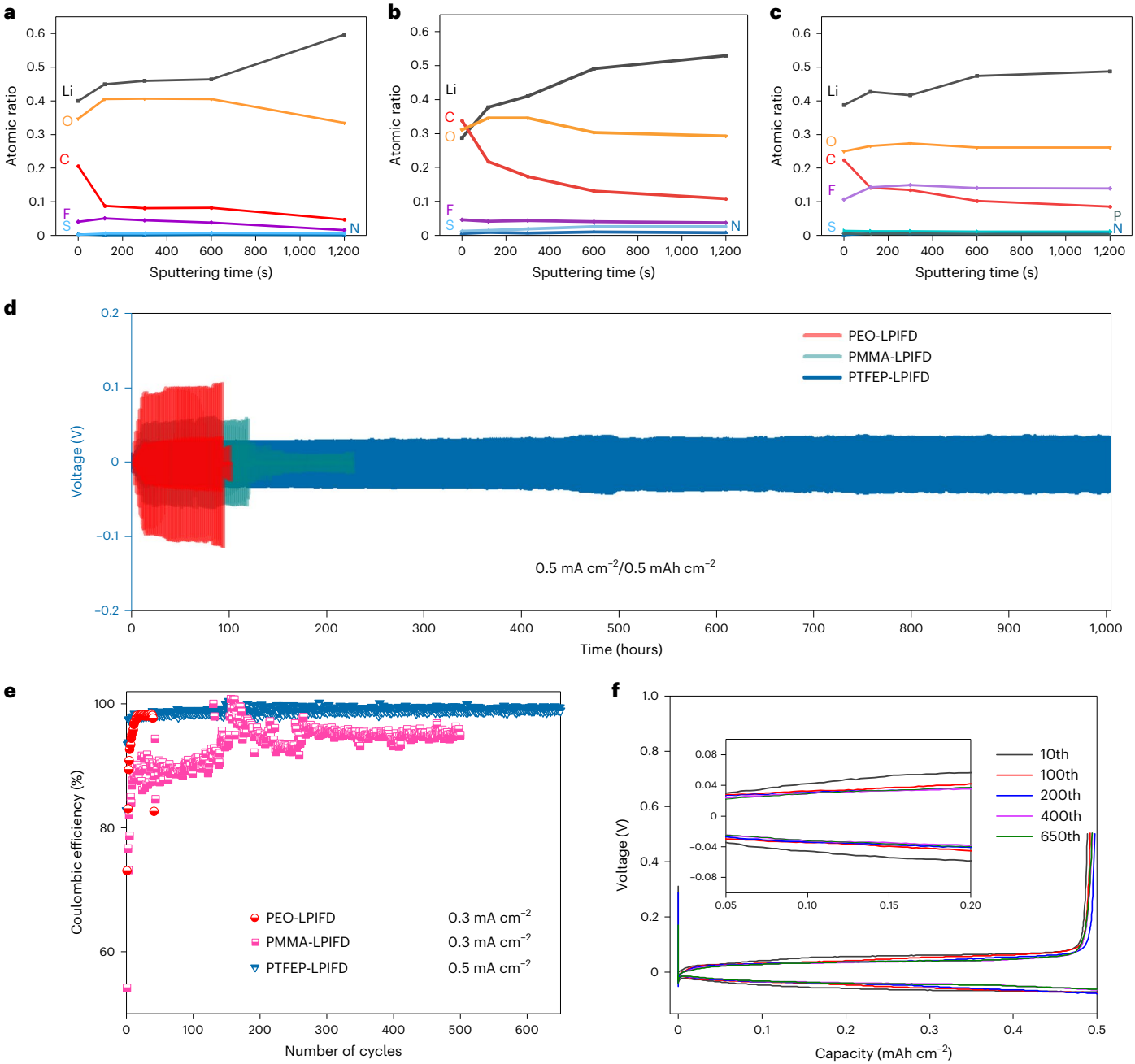

Fig. 4 | SEI composition and electrochemical performance of LPIFD polymer electrolytes with lithium. a–**c**, Quantified atomic composition ratios of the SEI at different sputtering times (0, 120, 300, 600 and 1,200 s from top to bottom) for PEO-LPIFD (**a**), PMMA-LPIFD (**b**) and PTFEP-LPIFD (**c**). **d**, Cycling profile for Li symmetric cells of Li|PEO-LPIFD|Li, Li|PMMA-LPIFD|Li and Li|PTFEP-LPIFD|Li at a current density of 0.5 mA cm^{-2} with 1 h/1 h plating/stripping time. **e**, CE of PEO-LPIFD (0.3 mA cm^{-2}), PMMA-LPIFD (0.3 mA cm^{-2}) and PTFEP-LPIFD (0.5 mA cm^{-2}). **f**, Li-metal plating/stripping profiles of a Li|PTFEP-LPIFD|Cu cell. The inset is an enlargement of part of the charge/discharge curve of 10th, 100th, 200th, 400th and 650th cycles.

inertness of PVDF-HFP and implying the non-uniform SEI formed in phase-separated LPIFD.

In contrast to the non-uniform SEI observed in PEO-LPIFD and the organic-rich SEI in PMMA-LPIFD, the atomic ratio of different elements in the SEI of PTFEP-LPIFD is almost constant from the surface to the inner SEI (Fig. 4c), and the peak intensities of different compositions are consistent at different depths (Supplementary Figs. 31c–34c). Moreover, relatively fewer C signals and higher F signals were detected in SEI, indicating an organic-less fluorinated SEI due to the high inorganic element ratio in PTFEP. In particular, a much stronger LiF peak was observed in the SEI of PTFEP-LPIFD (Supplementary Fig. 33c). The homogeneous LiF-rich SEI structure in PTFEP-LPIFD is attributed to the uniform distribution of PTFEP in the PVDF-HFP. LiF, being highly lithiophobic with weak bonding and high interfacial energy with Li metal, suffers less stress and retains good mechanical strength during Li plating/stripping, promoting the lateral deposition of metallic Li and suppressing the growth of Li dendrites[73]. As a result, the homogeneous, organic-less and LiF-rich SEI in PTFEP-LPIFD substantially contributes to suppressing Li dendrites[20].

The distinctive structural features (with or without phase boundaries) and SEI chemistry of the three LPIFDs result in the different Li-dendrite suppression abilities and Li plating/stripping CEs. The Li-dendrite suppression was evaluated using the CCD and the cycling stability in symmetric Li||Li cells. For PEO-LPIFD, short-circuiting was

quickly observed at 0.6 mA cm^{-2} (Supplementary Fig. 35a). Although PEO itself has high stability against Li metal and forms organic-less SEI due to the ether-based functional group, the phase separation results in non-uniform Li deposition and SEI formation, allowing Li dendrites to grow along the phase boundaries between PEO and PVDF-HFP. PMMA is fully miscible with PVDF-HFP and forms a single-phase LPIFD. However, the ester-based functional group of PMMA forms an organic-rich SEI that promotes Li-dendrite formation, especially at high current densities. Therefore, short-circuiting is observed when the current density reaches 1.4 mA cm^{-2} (Supplementary Fig. 35b). In sharp contrast, PTFEP-LPIFD, with its single-phase structure and LiF-rich SEI, shows no short-circuiting until a high current of 3.7 mA cm^{-2} (Supplementary Fig. 35c). The Li||Li cell with PTFEP-LPIFD was also tested under an increasing current density from 0.5 to 8.5 mA cm^{-2} at a fixed capacity of 0.5 mAh cm^{-2} (Supplementary Fig. 36). The results indicate its potential for high-current-density applications. Figure 4d illustrates the cycling stability of Li||Li cells using the three LPIFDs at a current of 0.5 mA cm^{-2} for 1 h charge/discharge. PTFEP-LPIFD exhibits much longer cycling stability compared to PEO-LPIFD and PMMA-LPIFD. The results of an additional Li||Li test are illustrated in Supplementary Fig. 37.

To directly assess the effectiveness of Li-dendrite suppression in a single-phase structure and LiF-rich SEI, we examined the morphology of three LPIFD membranes after Li||Li cycling and identified Li dendrites inside the solid electrolytes using solid-state ^{7}Li NMR spectra with magic angle spinning[74–76]. The PEO-LPIFD sample revealed visible metallic Li on both the surface and inner regions (Supplementary Fig. 38a), indicating the growth of Li dendrites into the PEO-LPIFD due to the phase separation. In contrast, only a few dark spots, referred to as 'dark lithium', were observed in single-phase PMMA-LPIFD and PTFEP-LPIFD (Supplementary Fig. 38b,c). The more pronounced decomposition in PMMA-LPIFD is attributed to the higher organic content in the SEI, in contrast to the PTFEP-LPIFD, which forms an LiF-rich SEI and exhibits enhanced stability. In the NMR spectra of PEO-LPIFD, a prominent ^{7}Li NMR signal at 264 ppm (green star in Supplementary Fig. 39a) was observed in cycled PEO-LPIFD, but this was absent in the fresh PEO-LPIFD, indicating that there was serious lithium-dendrite growth within the PEO-LPIFD. Conversely, only a weak peak corresponding to metallic lithium was observed in the amplified spectra of cycled PMMA-LPIFD and PTFEP-LPIFD (Supplementary Fig. 39b,c). The robust Li-dendrite suppression for the single-phase structure and LiF-rich SEI is further supported by the bulky and smooth lithium morphology (Supplementary Fig. 40) as well as the cell electrochemical impedance (Supplementary Fig. 41) for PTFEP-LPIFD electrolytes after cycling (additional details in Supplementary Note 7).

The Cu||Li half cells were used to investigate the Li plating/stripping CE. The Li CE is mainly controlled by whether the phase is single or separated and by the SEI chemistry. As shown in Fig. 4e (red) and Supplementary Fig. 42a, the CE of PEO-LPIFD at a low current density of 0.3 mA cm^{-2} can quickly reach 98% due to the good stability of the ether group of PEO and organic-less SEI. However, phase separation leads to a quick short circuit (Supplementary Fig. 42a). The single-phase PMMA-LPIFD shows a much longer cycling stability (Supplementary Fig. 42b), but the Li CE could reach only 95% at the same current of 0.3 mA cm^{-2} after 300 cycles (Fig. 4e, pink). The low Li CE of PMMA-LPIFD is attributed to the organic-rich SEI generated by the reduction of the ester group in PMMA. When the current density was increased to 0.5 mA cm^{-2}, the cell short-circuited within 100 cycles and the Li CE was further reduced (Supplementary Fig. 43). In sharp contrast, even at a current density of 0.5 mA cm^{-2}, the Li||Cu half-cell using PTFEP-LPIFD reached a high CE ≈ 99.1% after 300 cycles (Fig. 4e, blue; for more CE test results, see also Supplementary Fig. 44). A long cycle with stable voltage polarization was also observed (Fig. 4f).

The morphology of Li metal deposited onto Cu was also investigated. At a current density of 0.3 mA cm^{-2} and a capacity of 0.6 mAh cm^{-2}, the top view of the deposited Li shows a nodule-like structure rather than a whisker-like dendrite structure (Fig. 5a,b), which agrees with the organic-less SEI in PEO-LPIFD. However, phase separation between PEO and F diluter results in non-uniform Li plating. A cross-sectional image of deposited Li shows that it has a thickness of 9.2 µm with a non-uniform structure and numerous holes (Fig. 5c). For PMMA-LPIFD, the morphology of deposited lithium exhibits a whiskery structure (Fig. 5d,e), which is consistent with its low CE of 95%. A cross-sectional image of Li after plating of 1.0 mAh cm^{-2} shows that it has a thickness of 9.0 µm with a loosely packed structure (Fig. 5f). In sharp contrast, the Li after plating for 2.0 mAh cm^{-2} using PTFEP-LPIFD exhibited a very dense surface with a compact structure and a thickness of 10.1 µm (Fig. 5g–i). This chunky Li was deposited with low tortuosity and an intimate connection to maintain the bulk integrity, as the robust LiF-rich SEI prevented the growth of dendrites in the deposited Li[57,77,78].

To comprehensively demonstrate the design criteria (aiming for a single-phase structure and LiF-rich SEI), we conducted tests with additional polymers in Fig. 2 and summarized the results in the table in Fig. 5j. Like PEO, PPC is immiscible with PVDF-HFP, resulting in a phase-separated PPC-LPIFD (Supplementary Fig. 45). In addition, the reduction of polycarbonate forms an organic-rich SEI compared to PEO-LPIFD. As a result, the PPC-LPIFD has the lowest CCD (0.3 mA cm^{-2}) and CE (<90%) (Supplementary Fig. 45) among these polymer blends. In contrast, PVSF is miscible with PVDF-HFP. An almost inorganic structure contributes to an organic-less SEI. Therefore, PVSF achieves both a higher CE (99%) and a higher CCD (2.4 mA cm^{-2}) (Supplementary Fig. 46). Overall, the formation of a LiF-rich and organic-less SEI with a single-phase structure underscores the excellent stability of single-phase LPIFD with Li and its superior lithium-dendrite suppression.

Performance of Li//NMC811 full cells at high voltage

Like liquid localized high-concentration electrolytes, a high concentration of LiFSI and a high ratio of F in LPIFD enables LPIFD to achieve high anodic stability, supporting the high-voltage cathode (NMC811). As shown in Fig. 6a, PTFEP-LPIFD exhibited anodic decomposition above 4.9 V, which increased to 5.4 V after two passivation cycles[30,79]. Note that the utilization of SPEs with high-voltage cathodes has traditionally been limited to a voltage of 4.3 V (refs. 30,79).

The electrochemical behaviour of NMC811 using PTFEP-LPIFD was evaluated in Li||NMC811 coin cells with excess Li and an aggressive cutoff voltage of 2.8–4.5 V. The NMC811 cathode's areal capacity was around 1–1.3 mAh cm^{-2}. As shown in Fig. 6b,c, the NMC811 in PTFEP-LPIFD delivers a very high initial CE (ICE) of 93.95%, and the CE quickly reached >99.9% within five cycles, indicating that a robust CEI quickly formed on the NMC811 surface with minimal capacity loss during the CEI formation. Moreover, the cell had a superior cycle life of >400 cycles (80% retention) at 0.5C with a high average CE of 99.95% (Fig. 6c) and little decay of the average voltage (Fig. 6d), indicating excellent stability at high voltage. To verify the scalability, a pouch cell was assembled using NMC811 and 20 um Li foil (negative/positive electrode capacity ratio N/P = 4.3) with a PTFEP-LPIFD electrolyte (Fig. 6e). After five pre-cycles, there was no obvious capacity fading over 100 cycles at 0.3C, and the average CE remained high at 99.945%, consistent with the good performance observed in coin cells with thin Li (Supplementary Figs. 47 and 48).

Fast charging of batteries is crucial for electric vehicles, but it remains an unresolved challenge. Achieving fast charging in a Li||NMC811 battery with SPEs is particularly challenging due to larger overpotential and poorer contacts compared to liquid electrolytes. Therefore, the high-voltage stability of the SPEs is extremely important for fast charging because a high cutoff charging voltage can offset the large overpotential at high current density, thereby mitigating the capacity loss attributed to the overpotential. Here, PTFEP-LPIFD

https://doi.org/10.1038/s41560-023-01443-0

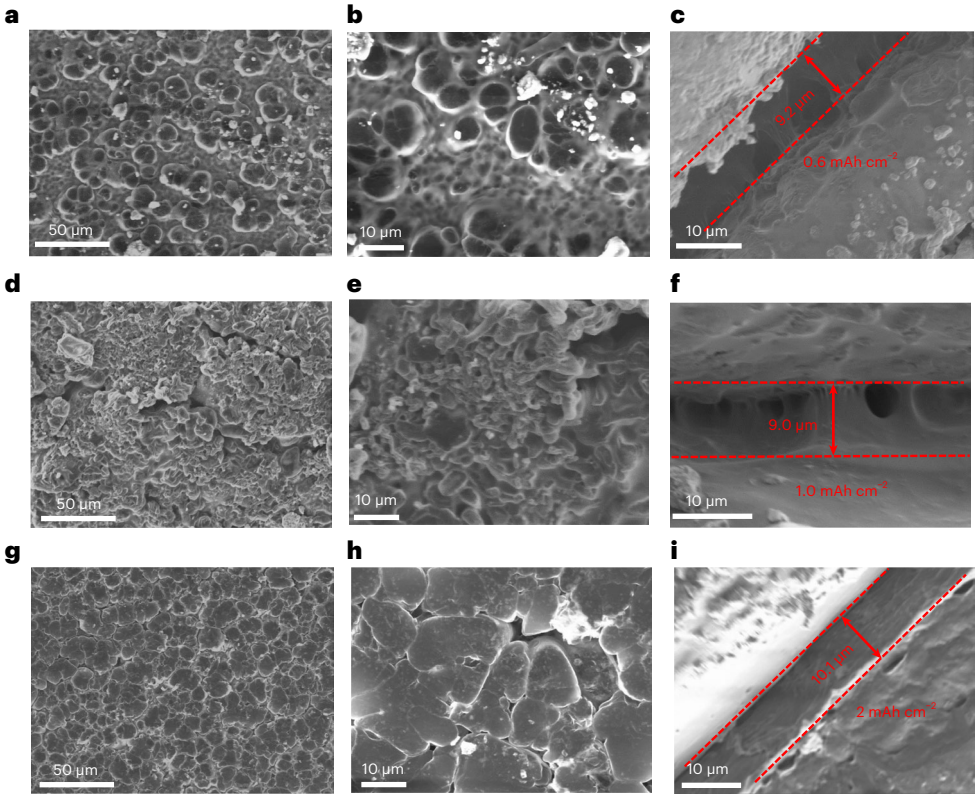

j

Property	Li-polymer PPC	Li-polymer PEO	Li-polymer PMMA	Li-polymer PVSF	Li-polymer PTFEP
SEI	Organic-rich	Organic-less	Organic-rich	Organic-less	Organic-less, LiF-rich
Single-phase (LPIFD)	No	No	Yes	Yes	Yes
CCD (mA cm^{-2})	0.3	0.6	1.4	2.4	3.7
CE	<90%	~98	~95	~99	~99

Fig. 5 | Different Li deposition behaviours of LPIFDs, and summary of design criteria. a–i, Surface and cross-section morphology of metallic Li deposited on the Cu substrate for PEO-LPIFD (0.3 mA cm^{-2}, 0.6 mAh cm^{-2}) (**a–c**), PMMA-LPIFD (0.3 mA cm^{-2}, 1 mAh cm^{-2}) (**d–f**) PTFEP-LPIFD (0.5 mA cm^{-2}, 2 mAh cm^{-2}) (**g–i**). To ensure consistency, the current density used for deposition is the same as that of the CE test. **j**, Table summarizing Li||Cu CEs and CCDs of different LPIFDs with different Li-polymers.

demonstrated remarkable stability at a high voltage of 4.6 V, reflected by a high-capacity retention of 79.7% after 200 cycles with an average CE of 99.91% for Li||NMC811 cells (Supplementary Fig. 49a). Moreover, the CE reached 99.94% at a high rate of 1C (Supplementary Fig. 49b). This high stability at high voltage allows PTFEP-LPIFD to support Li||NMC811 cells at a high cutoff voltage in delivering a high capacity at a high C rate. As illustrated in Fig. 6f and Supplementary Fig. 50a, if the Li||NMC811 cell is limited to being charged only up to 4.35 V, a reversible specific capacity of 148.7 and 77 mAh g^{-1} can be delivered at a rate of 1C and 2C, respectively. The much lower capacity at 2C is attributed to the overpotential and contact issues associated with polymer electrolytes. In comparison, the Li|PTFEP-LPIFD|NMC811 cell with a cutoff voltage of 4.6 V delivered high reversible specific capacities of 186 and 101.2 mAh g^{-1} at 1C and 2C, respectively. At a higher working temperature of 45 °C, by charging to 4.6 V, the cell can even work at 2C, 3C and 4C with high reversible capacities of 202.2, 146.7 and 105 mAh g^{-1} (Fig. 6f and Supplementary Fig. 50b, additional high-rate data are shown in Supplementary Fig. 51).

The high stability and high-rate capability observed in NMC811 can be attributed to the thin (<2 nm) and uniform CEI in single-phase PTFEP-LPIFD (Fig. 6g). The cycled NMC811 particle surface maintains a layered structure without rock-salt structure, indicating that the detrimental phase transition was effectively suppressed with PTFEP-LPIFD. The thickness of this highly stable CEI remained unchanged even after 200 cycles (Supplementary Fig. 52), which is also supported by the steady resistance evolution of Li|PTFEP-LPIFD|NMC811 full cells (Supplementary Fig. 53). XPS measurements were conducted to analyse the CEI composition. Compared to a cathode cycled in commercial carbonate electrolytes (1 M $LiPF_6$ in ethylene carbonate/diethyl carbonate, Supplementary Fig. 54a–c), NMC811 cycled in PTFEP-LPIFD has a much stronger F signal owing to the high F content ratio in this LPIFD (Supplementary Fig. 54e). Moreover, notably fewer O signals were observed (Supplementary Fig. 54d,f), indicating the excellent suppression of oxygen dissolution on the cathode. Thermodynamically, these fluorine-containing species are much more resistant to oxidation than oxide species, which effectively suppress the side reaction on the cathode.

https://doi.org/10.1038/s41560-023-01443-0

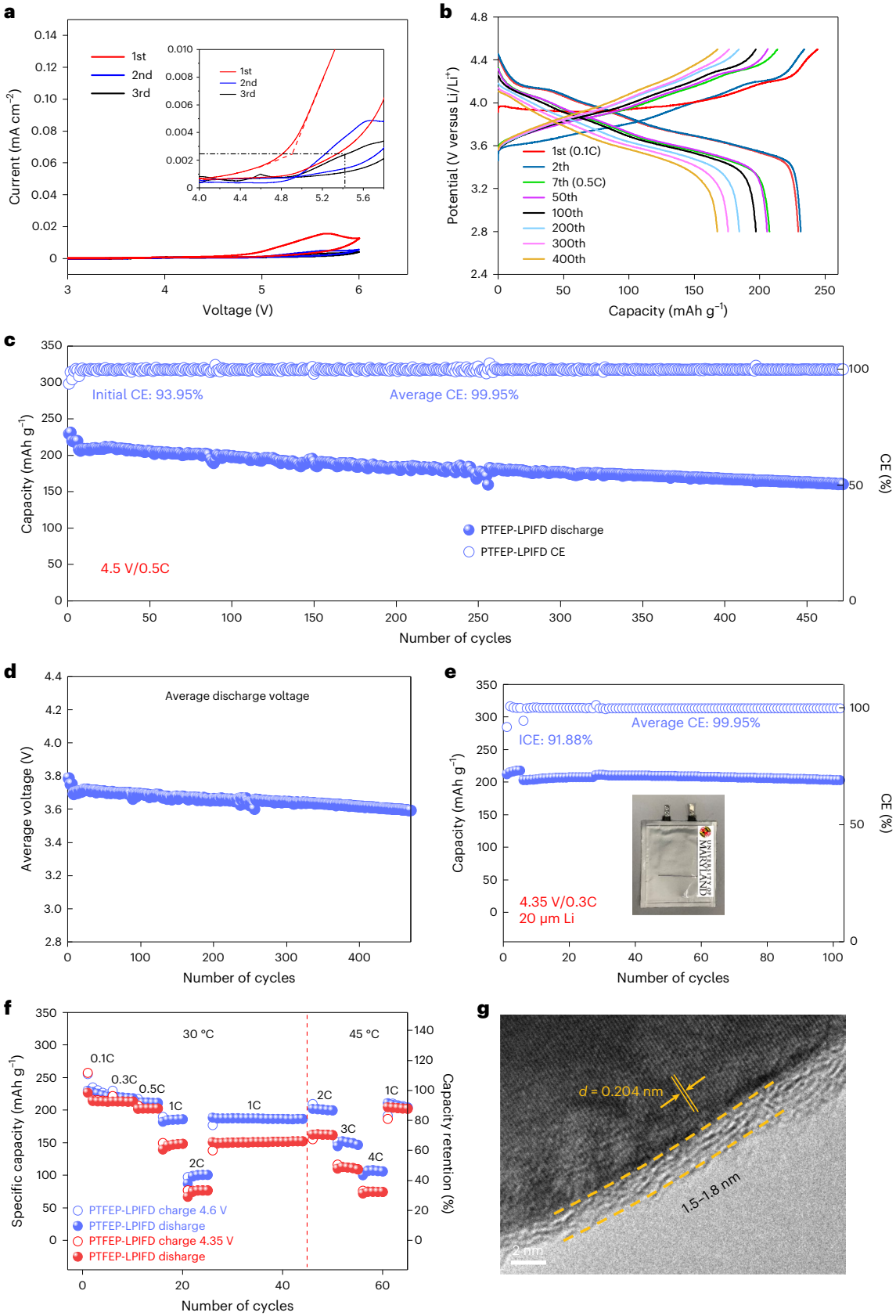

Fig. 6 | Full-cell performance of single-phase LPIFD. a, Electrochemical stability window of PTFEP-LPIFD. The inset is an enlargement of part of the curve. **b**–**d**, Voltage profiles (**b**), cycling performance (**c**) and average discharge voltage (**d**) of the coin cells with NMC811 cathodes at 4.5 V cutoff voltage using PTFEP-LPIFD. **e**, Cycling performance of the homemade pouch cell (N/P = 4.3) with 20 μm Li foil at 4.35 V cutoff voltage using PTFEP-LPIFD. The dimension of the electrode in the pouch cell is 3.7 cm × 3.7 cm. The C rate is 0.3C. The inset is a photograph of the cell. **f**, Rate performance (1C = 200 mAh g^{-1}, with capacity retention at right y axis) at 30 °C and 45 °C at 4.35 V versus 4.6 V cutoff voltages using PTFEP-LPIFD. During the rate test, both cells were charged to 4.6 V in the first cycle to ensure that the same CEI formed. **g**, TEM images of cycled NMC811 electrodes collected from Li|PTFEP-LPIFD|NMC811 cell after 100 cycles. ICE, initial CE.

Versatility of LPIFDs

By preventing dendrite growth and high-voltage decomposition, our single-phase LPIFDs exhibit excellent interfacial stability at both electrodes. They have good mechanical properties and can be fabricated easily. For these reasons, LPIFDs are attractive for various solid-state batteries (details in Supplementary Note 8). Ceramic electrolytes inherently possess grain boundaries that can facilitate Li-dendrite growth. Single-phase LPIFD can serve as an interlayer that prevents dendrites from growing through grain boundaries, leading to an improved CE of over 98% and a high CCD of 3.7 mA cm^{-2} (Supplementary Figs. 55 and 56), allowing the Li||NMC811 full cell to achieve 150 cycles (Supplementary Fig. 57). Furthermore, an LPIFD can serve as the binder for polymer/ceramic hybrid composites, which allows for thin Li_6PS_5Cl (LPSC) membranes having good stability with Li metal (Supplementary Figs. 58–61) and thereby enhance full-cell performance (Supplementary Fig. 62). An LPIFD can also be used in a cell with micro-sized Si, which can be cycled over 400 times (Supplementary Fig. 63). In this case, the LPIFD acts as a buffer against volume expansion and forms LiF-rich SEI to stabilize the Si anode.

Conclusions

We have designed single-phase, locally high-concentration polymer electrolytes due to the high miscibility between Li-polymer and an inert fluorinated diluter polymer. The single-phase LPIFD lacks phase boundaries, facilitating uniform Li deposition and ensuring a homogeneous LiF-rich SEI to stabilize the Li anode. Simultaneously, an F-rich CEI is formed to stabilize the NMC811 cathode at high voltage. As a result, the LPIFD achieves a high CE of 99.1% and a high CCD of 3.7 mA cm^{-2} on Li anodes, along with a high CE of 99.95% at 4.5 V with a cycle life exceeding 450 cycles in Li||NMC811 cells. Moreover, Li||NMC811 cells can be charged to 4.6 V with a high rate of up to 4C at 45 °C. The LPIFD concept can be extended to other solid-state electrolytes (for example, ceramics) and in batteries with other electrodes (for example, micro-sized Si anodes). Thus, LPIFDs could prove to be the electrolytes of choice for a range of high-energy batteries.

Methods

Materials and methods

Materials and preparation of electrolytes. LiFSI was purchased from Nippon Shokubai. PVDF-HFP (pellets), PPC (average Mn ~50,000, pellets), PEO (viscosity average molar mass of 100,000, powder), PMMA (average molecular weight of ~15,000, powder) and poly(bis(2,2,2-trifluoroethoxy)phosphazene) (PTFEP, powder) were purchased from Sigma-Aldrich. All were dried at 90 °C under vacuum for 24 h to remove moisture. Ethenesulfonyl fluoride was used to synthesize the PVSF by the reported method[80,81]. Basic information about these polymers (T_g and T_m) is listed in Supplementary Table 1. Acetonitrile (AN; ≥99.9%, boiling point 82 °C) and DME (99.9%, inhibitor-free, boiling point 85 °C) were bought from Sigma-Aldrich and dried overnight using molecular sieves.

All the fabrication processes, including the preparation of polymer electrolytes and the assembly of batteries, were done in an Ar-filled glovebox with H_2O content <0.1 ppm to avoid moisture in the air. The LPIFDs were made by the solution cast method. DME can dissolve most of the polymers in this work, thereby enhancing the accuracy of comparisons of different polymer electrolytes. In detail, all polymers (PMMA, PTFEP, PPC, PVSF and PVDF-HFP) were dissolved separately in DME at a concentration of 5 wt% (PVDF-HFP had to be dissolved by stirring it on a hot plate at 55 °C). In all cases, transparent polymer solutions were obtained. Because of the limited solubility of PEO in DME, PEO alone was dissolved in the AN at 3 wt%. Thereafter, the solution of PEO, PMMA, PTFEP, PPC or PVSF (Li-polymer) was mixed with the solution of PVDF-HFP (F diluter) at a weight ratio of 1:2.5 to get the solution of polymer blends. Then the LiFSI (63 wt% in LPIFD) was added into the polymer blend solution to get the LPIFD solution. The LPIFD solutions were then poured into Teflon dishes and dried at room temperature to evaporate most of the DME, then these membranes were further dried in a vacuum oven at 70 °C overnight and 75 °C for 2–3 h to remove solvents. The LPIFD SPEs were then peeled off from the dishes and cut into different sizes for testing.

The LPSC solid electrolyte was prepared by milling Li_2S, P_2S_5 and LiCl at a stoichiometric ratio followed by annealing at 550 °C for 4 h. LPSC pellets were made by pressing the LPSC electrolyte at 360 MPa. The PTFEP-LPIFD interlayer was formed by dropping 60–80 µl of LPIFD solution onto the surface of a LPSC pellet (20 µl per time), followed by drying using the same conditions as above for forming LPIFD membranes.

An LPSC membrane with a polytetrafluoroethylene (PTFE) binder was made as follows. The LPSC powder was hand milled with 1% PTFE and roll-pressed into a free-standing sheet. Then the sheet was pressed at 360 MPa to obtain thin solid electrolytes.

An LPSC membrane with a LPIFD binder was made as follows. The LPSC powder was well dispersed into the PTFEP-LPIFD precursor solution, then the suspension was poured onto a Teflon dish and dried quickly at a high temperature of 70 °C and in vacuum. To improve the mechanical properties, we used a lower salt content (53 wt% LiFSI). Then the sheet was pressed at 360 MPa to obtain thin solid electrolytes.

The composite cathode was created by directly filling a diluted polymer solution into the cathode and drying using the same process as above. Specifically, the LPIFD solution was diluted four times with DME, and then a certain amount of polymer solution was dropped onto a $LiNi_{0.8}Mn_{0.1}Co_{0.1}O_2$ (NMC811) cathode in multiple times and dried together with LPIFD. An uncalendered NMC811 cathode (95 wt% active materials) coated on Al foil with a loading of around 1–1.3 mAh cm^{-2} at 4.5 V was kindly provided by Saft America, Inc. A cathode with a loading of 2–3 mg cm^{-2} was used for the high-rate cycling test.

To coat the micro-silicon electrodes, a slurry was first prepared by dispersing silicon (Si) particles (average particle size 1–5 µm, 99.9% metals basis), lithium polyacrylate binder (10 wt% aqueous solutions) and C65 carbon black in water with a weight ratio of 6:2:2. The slurry was cast onto a copper (Cu) foil, dried at room temperature for 24 h and further dried at 90 °C overnight under vacuum. A composite Si-LPIFD anode was made by combining the Si anode with a diluted LPIFD solution in a manner identical to that used to make the composite cathode.

Electrochemical measurements. The ionic conductivities of LPIFD membranes at different temperatures (25–80 °C) were determined by electrochemical impedance spectroscopy over a frequency range of 1.0 MHz to 0.1 Hz on a Gamry workstation (Gamry Instruments, Inc.) using SS|LPIFD|SS coin cells (SS, stainless steel electrodes). The ionic conductivities were calculated as follows:

$$\sigma = \frac{L}{RS}, \tag{1}$$

where L is the thickness of the LPIFD, R is the resistance of the bulk electrolyte and S is the effective contacting area between the electrolyte and SS electrodes. The transference number t_+ was calculated as follows:

$$t_+ = \frac{I_S\,(\Delta V - I_0 R_0)}{I_0\,(\Delta V - I_S R_S)}, \tag{2}$$

where ΔV is the voltage polarization applied, I_S and R_S are the steady-state current and resistance, respectively, and I_0 and R_0 are the initial current and resistance, respectively.

The cyclic voltammogram of the Li|LPIFD|Ti cells was measured with a scan rate of 1 mV s^{-1} on an electrochemical workstation (CHI 600E, CH Instruments). The interfacial stability of Li-electrolyte was measured for a symmetric cell (Li|LPIFD|Li) with Li with a diameter

of 8 mm. The CE of metallic Li was calculated using Li|LPIFD|Cu. Rough copper was used to increase the contact between the polymer electrolytes and Cu. The electrochemical performances of the Li-metal batteries were all examined using 2032-type coin cells, which were assembled and disassembled in an Ar-filled glovebox with O_2 and a moisture content lower than 1 ppm. All the charge and discharge processes of Li||Cu, Li symmetrical and Li||NCM811 full cells were tested with a battery testing system (Landt Instruments) at 30 or 35 °C when there was no specific comment. For galvanostatic tests of NMC811|LPIFD|Li cells, Ti was used to prevent the corrosion of LiFSI on the stainless steel when charging to the high voltage. Thus, 14 mm of Ti was placed between the cathode and coin cell case. NCM811 cathodes with diameters of 9 or 9.5 mm were coupled to a 12 mm polymer membrane so that the polymer membrane was not in contact with the coin cell case at the cathode side. For the thin Li, a larger diameter of Li was used to prevent contact between the cathode and anode. The cells were charged and discharged between the voltage ranges 2.8–4.35 V, 2.8–4.5 V and 2.8–4.6 V. Two formation cycles at C/10 were first conducted before long-term cycling at a higher current density of C/2. Cyclic voltammetry and electrochemical impedance spectroscopy were all conducted on an electrochemical workstation (CHI 600E, CH Instruments). A two-electrode Li|LPSC|Li symmetric cell was assembled in a solid-state cell mould by attaching Li foil on both sides of the electrolyte pellet. The stack pressure was about 2.0 MPa. For LPSC with a PTFEP-LPIFD interlayer, both Li||Li and composite NMC811||Li cells were tested in coin cells due to the good contact between the electrolyte and the lithium.

Characterization. FTIR was recorded by a NEXUS 670 FTIR instrument. The morphologies were characterized using SEM. The SEM and high-resolution transmission electron microscopy (TEM) images in the present work were taken at the University of Maryland using a scanning electron microscope (SU-70 Analytical, GEG Hitachi) and a transmission electron microscope (JEM-2100 LaB6, JEOL) with an electron accelerating voltage of 200 keV. After cycling, all the electrodes were rinsed in DME (DME/AN for PEO-LPIFD) several times to remove any residual polymer electrolytes. XPS measurements were acquired with a K-alpha Thermo system using Al Kα radiation ($h\nu$ = 1,486.6 eV) under ultra-high vacuum (<1 × 10−12 atm) with a measured spot size of 400 µm in diameter. A flood gun was used during the analysis to compensate for the charging of the samples. The samples were transferred from the argon glovebox into the XPS chamber with a vacuum transfer vessel to avoid exposure to air. Sputter depth profiling was carried out using an Ar^+ ion gun with ion energy of 200 eV and a roster size of 2 mm. The angle between the surface normal and the ion gun beam was 0°. The sputter procedure was applied four times for 120 s, 300 s, 600 s and 1200 s. The binding energy was corrected based on the C 1*s* spectrum, assigning C–C to 284.8 eV. Relative atomic concentrations were calculated by integrating respective peaks with a Shirley background using the CasaXPS software to account for the respective atomic sensitivity factors.

STXM measurements were performed at the SM beamline of the Canadian Light Source. The polymer electrolyte was spin-coated on Si_3N_4 windows for the STXM at the C, O and F K-edges. In STXM, a monochromatic X-ray beam was focused by a Fresnel zone plate to a 30 nm spot on the sample, and the sample was raster-scanned with synchronized detection of the transmitted X-rays to generate image sequences (stacks) over a range of photon energies. The obtained STXM data were analysed using aXis2000 (http://unicorn.mcmaster.ca/aXis2000.html). The principal component analysis and the following cluster analysis of the STXM data were performed using the PCA_GUI 1.1.1 (Stony Brook University) free software[82].

The total electron yield of oxygen K-edge XAS spectra in the soft XAS was measured at the 23-ID-2 beamline (IOS) of National Synchrotron Light Source II, Brookhaven National Laboratory. The data were analysed using the Athena software[83].

All rheological experiments were done with a rheometer (HR 20 Discovery Hybrid Rheometer, TA Instruments) at 60 or 100 °C using a parallel-plate geometry (25 mm diameter). For the oscillatory shear experiments (dynamic rheology), polymer or SPE samples were cut into discs of 20 mm diameter. The linear viscoelastic region of the samples was obtained in stress-sweep experiments. A strain (0.5%) within this region was used to run the frequency-sweep experiments.

Quantification solution ^{1}H NMR experiments for all samples were run on a Bruker AVANCE III 600 MHz NMR spectrometer with a BBFO probe. The polymer electrolytes were dissolved in dimethyl sulfoxide at 50 °C for one night while being stirred. A one-pulse programme with a pulse delay of 30 s and 16 scans was employed to collect ^{1}H NMR spectra with reference to tetramethylsilane. Solid-state ^{7}Li NMR spectra with magic angle spinning of all samples were collected on a Bruker Avance NEO solid-state 500 MHz NMR spectrometer with a double resonance H/F-X probe. Briefly, samples were packed in a 3.2 mm outer diameter zirconia rotor with a Kel-F endcap spinning at 10 or 8 kHz. The one-pulse programme was used with a π/2 pulse length of 2.5 µs and a recycle delay of 5 s. Each ^{7}Li NMR spectrum was collected from 128 scans and the line broadening for the spectrum was 20 Hz. Each ^{7}Li NMR spectrum was referenced to 10 M LiCl in a D_2O solution by setting the ^{7}Li chemical shift at 0 ppm.

Computational details. In the classical molecular dynamics simulation, LPIFD systems composing three different polymer blends based on (1) PVDF-HFP, (2) conductive PEO, PMMA or PTFEP and (3) LiFSI salt were assembled in the same composition used in the experiment, namely 1:0.4:2.4. The non-polarizable all-atomic optimized potentials for liquid simulations (OPLS(-AA)) force field[84,85] as available in the database for the Gromacs simulation package[86–90], was utilized to adjust most of the intra- and intermolecular potential parameters that describe covalent terms for bond stretching, angle bending and dihedral angle torsion along the covalent bond. Non-covalent terms were represented by the van der Waals and Coulomb interactions. For PTFEP, all the missing intermolecular parameters related to the –P=N– bond were generated using a modified version of OPLS-AA(-M) (ref. 91) available from the LigParGen web service[92]. The Coulomb interactions were described by the partial charges evaluated in the Merz–Singh–Kollman scheme[93] based on the trimmer configuration. The latter was initially optimized using HF/6-31 G(d) level of theory, followed by an analysis in MP2/cc-pVTZ as available in Gaussian 16 (ref. 94).

A chain length of 50 monomers was selected for each polymer. To keep the amorphous structure of PVDF-HFP, the VDF to HFP molar ratio was set to 4:1 (refs. 95–98), while maintaining the VDF/HFP monomer sequence reported previously[95,98]. Each initial system containing ~50,000 atoms was generated by Packmol and placed into an orthorhombic box of size 20 × 20 × 60 nm^3 with three-dimensional periodic boundary conditions. This system size was selected to avoid deleterious pressure fluctuations and to reduce the influence of the finite size on the polymer dynamics and electrostatic interactions during the equilibration stage[99]. A considerably larger box was used to avoid intermolecular and interchain clashes.

All molecular dynamics simulations were carried out using Gromacs v.2016.3. The equations of motion were integrated using the leap-frog algorithm[100] with a time step of 2×10^{-6} ns. The time-step selection was justified due to the C–H bonds constraints, which were implemented with LINCS, a linear constraint solver algorithm[101]. The electrostatic long-range interactions within the cutoff range of 1.4 nm were accounted for by the computationally efficient particle mesh Ewald algorithm[102], using the same cutoff distance for the real-space component. The 12-6 Lennard-Jones interactions were treated by the conventional shifted force technique with a switch region between 1.2 and 1.3 nm. Cross interactions between different atom types were derived using the standard Lorentz–Berthelot combination rule.

The LPIFD systems considered were energy-minimized using the steepest descent algorithm followed by a series of equilibration steps in isothermal and isobaric (npT) and canonical (nVT) ensembles. To facilitate blending and to reduce the computational costs at certain steps, the temperature was increased by 230 or 330 K with respect to experimental conditions: (1) 0.1 ns of npT compression at 1 kbar and 533 K, (2) 0.1 ns of npT compression at 4 kbar and 533 K, (3) 0.5 ns of npT compression at 4 kbar and 533 K, (4) 1 ns of npT relaxation at 0.001 kbar and 533 K, (5) 0.5 ns of npT heating at 0.001 kbar and 633 K, (6) 0.5 ns of npT cooling at 0.001 kbar and 533 K, (7) 1 ns of nVT relaxation at 533 K;,(8) 6.3 ns of npT relaxation at 0.001 kbar and 533 K, (9) 1,000 ns of npT blending at 0.001 kbar and 533 K and (10) 200 ns of npT cooling 0.001 kbar and 303 K according to experimental conditions. For steps 1–8, the temperature and pressure were kept constant by applying the Berendsen thermostat and barostat[103] with coupling constants of 3×10^{-4} and 5×10^{-4} ns, respectively. For step 8, a velocity-rescaling[104] thermostat and Parrinello–Rahman barostat[105] were set with further substitution by a Nose–Hoover thermostat (8×10^{-4} ns) for the last two steps 9 and 10. All the structure properties presented in this work were derived from an additional 10 ns of nVT trajectory by saving the coordinates each 1×10^{-3} ns and additionally enhanced by the Travis code[106,107] version 21 May 2021.

The initial geometry configurations obtained from the molecular dynamic simulations were cut down to limit the polymeric repeating units to only two or three units of PMMA, PEO or PTFEP, which were in close proximity to (interacting with) the LiFSI. The cutdown was made to limit the computational costs when performing the quantum chemistry calculations. The generated structures were then optimized using the GFN2-XTB method[108], which is an accurate and broadly parametrized self-consistent tight-binding method. The optimized geometries were used to calculate the XAS spectra.

All calculations were performed using the ORCA software v.5.0.3 (ref. 109). The oxygen K-edge XAS spectra were calculated using DFT combined with the restricted open-shell configuration interaction with singles (DFT-ROCIS) method[110]. This method was chosen as several studies have reported it to be an excellent method for predicting experimental XAS measurements accurately[111]. Throughout our calculations, the B3LYP[112,113] functional was used with the Ahlrichs polarized def2-TZVP basis sets[114,115] together with the auxiliary def2/J (refs. 116,117) to accelerate the calculations in the presence of RIJCOSX approximations. Additionally, scalar relativistic effects were implemented by employing ZORA corrections[118] explicitly. Scaling parameters c1 = 0.18, c2 = 0.20 and c3 = 0.40 were used as they were proven to be the best set of parameters for a chosen test set[110]. The excitation window was constructed by specifying one donor space corresponding to the excitation donor orbitals and an acceptor orbital space that corresponds to all singly occupied states and the entire virtual orbitals space. A total of 100 roots were requested to cover as many single excitation states as possible. The data files for generating plots were produced using a utility called Orca_mapspc that is integrated into the ORCA program suite. The peaks were normalized and a constant energy shift of +13.2 to +15 eV was made to match with the pre-edge peak energy positions of the experimental measurements.

Data availability

All data are available in the main text or the supplementary materials.

References

1. Lin, D., Liu, Y. & Cui, Y. Reviving the lithium metal anode for high-energy batteries. *Nat. Nanotechnol.* **12**, 194–206 (2017).
2. Lu, Y., Tu, Z. & Archer, L. A. Stable lithium electrodeposition in liquid and nanoporous solid electrolytes. *Nat. Mater.* **13**, 961–969 (2014).
3. Huang, W., Feng, X., Han, X., Zhang, W. & Jiang, F. Questions and answers relating to lithium-ion battery safety issues. *Cell Rep. Phys. Sci.* **2**, 100285 (2021).
4. Bai, P., Li, J., Brushett, F. R. & Bazant, M. Z. Transition of lithium growth mechanisms in liquid electrolytes. *Energy Environ. Sci.* **9**, 3221–3229 (2016).
5. Li, W. et al. The synergetic effect of lithium polysulfide and lithium nitrate to prevent lithium dendrite growth. *Nat. Commun.* **6**, 7436 (2015).
6. Ren, Y., Shen, Y., Lin, Y. & Nan, C.-W. Direct observation of lithium dendrites inside garnet-type lithium-ion solid electrolyte. *Electrochem. Commun.* **57**, 27–30 (2015).
7. Xu, K. Nonaqueous liquid electrolytes for lithium-based rechargeable batteries. *Chem. Rev.* **104**, 4303–4418 (2004).
8. Cheng, X.-B., Zhang, R., Zhao, C.-Z. & Zhang, Q. Toward safe lithium metal anode in rechargeable batteries: a review. *Chem. Rev.* **117**, 10403–10473 (2017).
9. Liu, S. et al. In situ solid electrolyte interphase from spray quenching on molten Li: a new way to construct high-performance lithium-metal anodes. *Adv. Mater.* **31**, 1806470 (2019).
10. Paul, P. P. et al. A review of existing and emerging methods for lithium detection and characterization in Li-ion and Li-metal batteries. *Adv. Energy Mater.* **11**, 2100372 (2021).
11. Park, R. J.-Y. et al. Semi-solid alkali metal electrodes enabling high critical current densities in solid electrolyte batteries. *Nat. Energy* **6**, 314–322 (2021).
12. Fan, X. et al. Fluorinated solid electrolyte interphase enables highly reversible solid-state Li metal battery. *Sci. Adv.* **4**, eaau9245 (2018).
13. Ji, X. et al. Solid-state electrolyte design for lithium dendrite suppression. *Adv. Mater.* **32**, 2002741 (2020).
14. Ren, Y. X. et al. Rational design of spontaneous reactions for protecting porous lithium electrodes in lithium–sulfur batteries. *Nat. Commun.* **10**, 3249 (2019).
15. Fan, X. et al. Non-flammable electrolyte enables Li-metal batteries with aggressive cathode chemistries. *Nat. Nanotechnol.* **13**, 715–722 (2018).
16. Wang, J. et al. Superconcentrated electrolytes for a high-voltage lithium-ion battery. *Nat. Commun.* **7**, 12032 (2016).
17. Yamada, Y. & Yamada, A. Superconcentrated electrolytes for lithium batteries. *J. Electrochem. Soc.* **162**, A2406 (2015).
18. Chen, J. et al. Electrolyte design for LiF-rich solid–electrolyte interfaces to enable high-performance microsized alloy anodes for batteries. *Nat. Energy* **5**, 386–397 (2020).
19. Fan, X. et al. Highly fluorinated interphases enable high-voltage Li-metal batteries. *Chem* **4**, 174–185 (2018).
20. Cao, X. et al. Monolithic solid–electrolyte interphases formed in fluorinated orthoformate-based electrolytes minimize Li depletion and pulverization. *Nat. Energy* **4**, 796–805 (2019).
21. Ren, X. et al. Localized high-concentration sulfone electrolytes for high-efficiency lithium-metal batteries. *Chem* **4**, 1877–1892 (2018).
22. Yu, Z. et al. Molecular design for electrolyte solvents enabling energy-dense and long-cycling lithium metal batteries. *Nat. Energy* **5**, 526–533 (2020).
23. Monroe, C. & Newman, J. The impact of elastic deformation on deposition kinetics at lithium/polymer interfaces. *J. Electrochem. Soc.* **152**, A396 (2005).
24. Monroe, C. & Newman, J. The effect of interfacial deformation on electrodeposition kinetics. *J. Electrochem. Soc.* **151**, A880 (2004).
25. Krauskopf, T., Richter, F. H., Zeier, W. G. & Janek, J. Physicochemical concepts of the lithium metal anode in solid-state batteries. *Chem. Rev.* **120**, 7745–7794 (2020).
26. Cao, D. et al. Lithium dendrite in all-solid-state batteries: growth mechanisms, suppression strategies, and characterizations. *Matter* **3**, 57–94 (2020).

27. Lu, Y. et al. Critical current density in solid-state lithium metal batteries: mechanism, influences, and strategies. *Adv. Funct. Mater.* **31**, 2009925 (2021).
28. Wang, Y. et al. Solid-state rigid-rod polymer composite electrolytes with nanocrystalline lithium ion pathways. *Nat. Mater.* **20**, 1255–1263 (2021).
29. Zhao, Q., Liu, X., Stalin, S., Khan, K. & Archer, L. A. Solid-state polymer electrolytes with in-built fast interfacial transport for secondary lithium batteries. *Nat. Energy* **4**, 365–373 (2019).
30. Cabañero Martínez, M. A. et al. Are polymer-based electrolytes ready for high-voltage lithium battery applications? An overview of degradation mechanisms and battery performance. *Adv. Energy Mater.* **12**, 2201264 (2022).
31. Lin, R. et al. Characterization of the structure and chemistry of the solid–electrolyte interface by cryo-EM leads to high-performance solid-state Li-metal batteries. *Nat. Nanotechnol.* **17**, 768–776 (2022).
32. Holoubek, J. et al. Tailoring electrolyte solvation for Li metal batteries cycled at ultra-low temperature. *Nat. Energy* **6**, 303–313 (2021).
33. Gao, H., Grundish, N. S., Zhao, Y., Zhou, A. & Goodenough, J. B. Formation of stable interphase of polymer-in-salt electrolyte in all-solid-state lithium batteries. *Energy Mater. Adv.* **2021**, 1932952 (2021).
34. Chen, F., Wang, X., Armand, M. & Forsyth, M. Cationic polymer-in-salt electrolytes for fast metal ion conduction and solid-state battery applications. *Nat. Mater.* **21**, 1175–1182 (2022).
35. Kimura, K., Yajima, M. & Tominaga, Y. A highly-concentrated poly(ethylene carbonate)-based electrolyte for all-solid-state Li battery working at room temperature. *Electrochem. Commun.* **66**, 46–48 (2016).
36. Fan, R. et al. Versatile strategy for realizing flexible room-temperature all-solid-state battery through a synergistic combination of salt affluent PEO and $Li_{6.75}La_3Zr_{1.75}Ta_{0.25}O_{12}$ nanofibers. *ACS Appl. Mater. Interfaces* **12**, 7222–7231 (2020).
37. Wang, X. et al. Lithium-salt-rich PEO/$Li_{0.3}La_{0.557}TiO_3$ interpenetrating composite electrolyte with three-dimensional ceramic nano-backbone for all-solid-state lithium-ion batteries. *ACS Appl. Mater. Interfaces* **10**, 24791–24798 (2018).
38. Wu, J. et al. Reducing the thickness of solid-state electrolyte membranes for high-energy lithium batteries. *Energy Environ. Sci.* **14**, 12–36 (2021).
39. Wang, X. *et al*. Ultra-stable all-solid-state sodium metal batteries enabled by perfluoropolyether-based electrolytes. *Nat. Mater.* **21**, 1057–1065 (2022).
40. Zhao, Y. et al. A rational design of solid polymer electrolyte with high salt concentration for lithium battery. *J. Power Sources* **407**, 23–30 (2018).
41. Cheng, X.-B., Zhao, C.-Z., Yao, Y.-X., Liu, H. & Zhang, Q. Recent advances in energy chemistry between solid-state electrolyte and safe lithium-metal anodes. *Chem* **5**, 74–96 (2019).
42. Han, F. et al. High electronic conductivity as the origin of lithium dendrite formation within solid electrolytes. *Nat. Energy* **4**, 187–196 (2019).
43. Wu, B. et al. The role of the solid electrolyte interphase layer in preventing Li dendrite growth in solid-state batteries. *Energy Environ. Sci.* **11**, 1803–1810 (2018).
44. Wu, Q. et al. Phase regulation enabling dense polymer-based composite electrolytes for solid-state lithium metal batteries. *Nat. Commun.* **14**, 6296 (2023).
45. Xi, J. et al. PVDF–PEO blends based microporous polymer electrolyte: effect of PEO on pore configurations and ionic conductivity. *J. Power Sources* **157**, 501–506 (2006).
46. Chaput, S., Carrot, C., Castro, M. & Prochazka, F. Co-continuity interval in immiscible polymer blends by dynamic mechanical spectroscopy in the molten and solid state. *Rheol. Acta* **43**, 417–426 (2004).
47. Liu, J. et al. Blending-based poly(vinylidene fluoride)/polymethyl methacrylate membrane for rechargeable lithium-ion batteries. *Ionics* **25**, 5201–5211 (2019).
48. Cznotka, E., Jeschke, S., Schmohl, S., Johansson, P. & Wiemhöfer, H.-D. 3D laser scanning confocal microscopy of siloxane-based comb and double-comb polymers in PVDF-HFP thin films. *J. Coat. Technol. Res.* **13**, 577–587 (2016).
49. Tang, L. et al. Polyfluorinated crosslinker-based solid polymer electrolytes for long-cycling 4.5 V lithium metal batteries. *Nat. Commun.* **14**, 2301 (2023).
50. Zhang, X. et al. Self-suppression of lithium dendrite in all-solid-state lithium metal batteries with poly(vinylidene difluoride)-based solid electrolytes. *Adv. Mater.* **31**, 1806082 (2019).
51. Liu, W. et al. Designing polymer-in-salt electrolyte and fully infiltrated 3D electrode for integrated solid-state lithium batteries. *Angew. Chem.* **133**, 13041–13050 (2021).
52. Zhang, W., Yi, Q., Li, S. & Sun, C. An ion-conductive $Li_7La_3Zr_2O_{12}$-based composite membrane for dendrite-free lithium metal batteries. *J. Power Sources* **450**, 227710 (2020).
53. Guo, S. et al. PVDF-HFP/LiF composite interfacial film to enhance the stability of Li-metal anodes. *ACS Appl. Energy Mater.* **3**, 7191–7199 (2020).
54. Borodin, O. Challenges with prediction of battery electrolyte electrochemical stability window and guiding the electrode–electrolyte stabilization. *Curr. Opin. Electrochem.* **13**, 86–93 (2019).
55. Yang, Z., Zhang, W., Li, J. & Chen, J. Polyphosphazene membrane for desulfurization: selecting poly[bis(trifluoroethoxy) phosphazene] for pervaporative removal of thiophene. *Sep. Purif. Technol.* **93**, 15–24 (2012).
56. Kaskhedikar, N. et al. Ionic conductivity of polymer electrolyte membranes based on polyphosphazene with oligo(propylene oxide) side chains. *Solid State Ion.* **177**, 703–707 (2006).
57. Jankowsky, S., Hiller, M. M. & Wiemhöfer, H.-D. Preparation and electrochemical performance of polyphosphazene based salt-in-polymer electrolyte membranes for lithium ion batteries. *J. Power Sources* **253**, 256–262 (2014).
58. Yu, Z. et al. Rational solvent molecule tuning for high-performance lithium metal battery electrolytes. *Nat. Energy* **7**, 94–106 (2022).
59. Xu, S. et al. Decoupling of ion pairing and ion conduction in ultrahigh-concentration electrolytes enables wide-temperature solid-state batteries. *Energy Environ. Sci.* **15**, 3379–3387 (2022).
60. Wang, J., Zhou, J., Hu, Y. & Regier, T. Chemical interaction and imaging of single Co_3O_4/graphene sheets studied by scanning transmission X-ray microscopy and X-ray absorption spectroscopy. *Energy Environ. Sci.* **6**, 926–934 (2013).
61. Schmeißer, D. et al. Characterization of oxidic and organic materials with synchrotron radiation based XPS and XAS. *Mater. Sci.* **27**, 141–157 (2009).
62. Widstrom, M. D. et al. Water domain enabled transport in polymer electrolytes for lithium-ion batteries. *Macromolecules* **54**, 2882–2891 (2021).
63. Chen, L. et al. A 63 m superconcentrated aqueous electrolyte for high-energy Li-ion batteries. *ACS Energy Lett.* **5**, 968–974 (2020).
64. Piao, N. et al. Countersolvent electrolytes for lithium-metal batteries. *Adv. Energy Mater.* **10**, 1903568 (2020).
65. Smith, J. W. et al. X-ray absorption spectroscopy of $LiBF_4$ in propylene carbonate: a model lithium ion battery electrolyte. *Phys. Chem. Chem. Phys.* **16**, 23568–23575 (2014).
66. Ong, M. T. et al. Lithium ion solvation and diffusion in bulk organic electrolytes from first-principles and classical reactive molecular dynamics. *J. Phys. Chem. B* **119**, 1535–1545 (2015).
67. Wu, C. H. et al. Molecular-scale structure of electrode–electrolyte interfaces: the case of platinum in aqueous sulfuric acid. *J. Am. Chem. Soc.* **140**, 16237–16244 (2018).

68. Yamane, H. et al. Critical absorbed dose of resinous adhesive material towards non-destructive chemical-state analysis using soft X-rays. *J. Electron Spectros. Relat. Phenom.* **232**, 11–15 (2019).
69. Zhou, D. et al. In situ synthesis of a hierarchical all-solid-state electrolyte based on nitrile materials for high-performance lithium-ion batteries. *Adv. Energy Mater.* **5**, 1500353 (2015).
70. Deng, T. et al. In situ formation of polymer-inorganic solid-electrolyte interphase for stable polymeric solid-state lithium-metal batteries. *Chem* **7**, 3052–3068 (2021).
71. Wu, N. et al. In situ formation of Li_3P layer enables fast Li^+ conduction across Li/solid polymer electrolyte interface. *Adv. Funct. Mater.* **30**, 2000831 (2020).
72. Fan, X. et al. All-temperature batteries enabled by fluorinated electrolytes with non-polar solvents. *Nat. Energy* **4**, 882–890 (2019).
73. Chen, J. et al. Electrolyte design for Li metal-free Li batteries. *Mater. Today* **39**, 118–126 (2020).
74. Bhattacharyya, R. et al. In situ NMR observation of the formation of metallic lithium microstructures in lithium batteries. *Nat. Mater.* **9**, 504–510 (2010).
75. Chandrashekar, S. et al. ^{7}Li MRI of Li batteries reveals location of microstructural lithium. *Nat. Mater.* **11**, 311–315 (2012).
76. Tsai, C.-L. et al. $Li_7La_3Zr_2O_{12}$ interface modification for Li dendrite prevention. *ACS Appl. Mater. Interfaces* **8**, 10617–10626 (2016).
77. Liu, S. et al. An inorganic-rich solid electrolyte interphase for advanced lithium-metal batteries in carbonate electrolytes. *Angew. Chem. Int. Ed.* **60**, 3661–3671 (2021).
78. Liu, S. et al. Salt-in-salt reinforced carbonate electrolyte for Li metal batteries. *Angew. Chem. Int. Ed.* https://doi.org/10.1002/anie.202210522 (2022).
79. Xu, K. Electrolytes and interphases in Li-ion batteries and beyond. *Chem. Rev.* **114**, 11503–11618 (2014).
80. Fujigaya, T. et al. New photoresist materials for 157-nm lithography. Poly[vinylsulfonyl fluoride-co-4-(1,1,1,3,3,3-hexafluoro-2-hydroxypropyl)-styrene] partially protected with *tert*-butoxycarbonyl. *Chem. Mater.* **15**, 1512–1517 (2003).
81. Gao, Y. et al. Polymer–inorganic solid–electrolyte interphase for stable lithium metal batteries under lean electrolyte conditions. *Nat. Mater.* **18**, 384–389 (2019).
82. Lerotic, M., Jacobsen, C., Schäfer, T. & Vogt, S. Cluster analysis of soft X-ray spectromicroscopy data. *Ultramicroscopy* **100**, 35–57 (2004).
83. Ravel, B. & Newville, M. ATHENA, ARTEMIS, HEPHAESTUS: data analysis for X-ray absorption spectroscopy using IFEFFIT. *J. Synchrotron Radiat.* **12**, 537–541 (2005).
84. Jorgensen, W. L. & Tirado-Rives, J. The OPLS [optimized potentials for liquid simulations] potential functions for proteins, energy minimizations for crystals of cyclic peptides and crambin. *J. Am. Chem. Soc.* **110**, 1657–1666 (1988).
85. Jorgensen, W. L., Maxwell, D. S. & Tirado-Rives, J. Development and testing of the OPLS all-atom force field on conformational energetics and properties of organic liquids. *J. Am. Chem. Soc.* **118**, 11225–11236 (1996).
86. Abraham, M. J. et al. GROMACS: High performance molecular simulations through multi-level parallelism from laptops to supercomputers. *SoftwareX* **1**, 19–25 (2015).
87. Pronk, S. et al. GROMACS 4.5: a high-throughput and highly parallel open source molecular simulation toolkit. *Bioinformatics* **29**, 845–854 (2013).
88. Hess, B., Kutzner, C., van der Spoel, D. & Lindahl, E. GROMACS 4: algorithms for highly efficient, load-balanced, and scalable molecular simulation. *J. Chem. Theory Comput.* **4**, 435–447 (2008).
89. van der Spoel, D. et al. GROMACS: fast, flexible, and free. *J. Comput. Chem.* **26**, 1701–1718 (2005).
90. Berendsen, H. J. C., van der Spoel, D. & van Drunen, R. GROMACS: A message-passing parallel molecular dynamics implementation. *Comput. Phys. Commun.* **91**, 43–56 (1995).
91. Robertson, M. J., Tirado-Rives, J. & Jorgensen, W. L. Improved peptide and protein torsional energetics with the OPLS-AA force field. *J. Chem. Theory Comput.* **11**, 3499–3509 (2015).
92. Dodda, L. S., Cabeza de Vaca, I., Tirado-Rives, J. & Jorgensen, W. L. LigParGen web server: an automatic OPLS-AA parameter generator for organic ligands. *Nucleic Acids Res.* **45**, W331–W336 (2017).
93. Singh, U. C. & Kollman, P. A. An approach to computing electrostatic charges for molecules. *J. Comput. Chem.* **5**, 129–145 (1984).
94. Tomasi, J. et al. Gaussian 16 Rev. C. 01 (Gaussian Inc., 2016).
95. Twum, E. B., McCord, E. F., Lyons, D. F., Fox, P. A. & Rinaldi, P. L. Characterization of end groups and branching structures in copolymers of vinylidene fluoride with hexafluoropropylene using multidimensional NMR spectroscopy. *Eur. Polym. J.* **51**, 136–150 (2014).
96. Apostolo, M., Arcella, V., Storti, G. & Morbidelli, M. Kinetics of the emulsion polymerization of vinylidene fluoride and hexafluoropropylene. *Macromolecules* **32**, 989–1003 (1999).
97. Ameduri, B., Boutevin, B. & Kostov, G. Fluoroelastomers: synthesis, properties and applications. *Prog. Polym. Sci.* **26**, 105–187 (2001).
98. Twum, E. B., McCord, E. F., Fox, P. A., Lyons, D. F. & Rinaldi, P. L. Characterization of backbone structures in poly(vinylidene fluoride-co-hexafluoropropylene) copolymers by multidimensional 19F NMR spectroscopy. *Macromolecules* **46**, 4892–4908 (2013).
99. Gartner, T. E. III & Jayaraman, A. Modeling and simulations of polymers: a roadmap. *Macromolecules* **52**, 755–786 (2019).
100. Hockney, R. W., Goel, S. P. & Eastwood, J. W. Quiet high-resolution computer models of a plasma. *J. Comput. Phys.* **14**, 148–158 (1974).
101. Hess, B., Bekker, H., Berendsen, H. J. C. & Lincs, J. F. A linear constraint solver for molecular simulations. *J. Comput. Chem.* **18**, 1463–1472 (1997).
102. Darden, T., & York, D. An $N \cdot \log(N)$ method for Ewald sums in large systems. *J. Chem. Phys.* **98**, 10089–10092 (1993).
103. Berendsen, H. J. C., van Postma, J. P. M., van Gunsteren, W. F., DiNola, A. & Haak, J. R. Molecular dynamics with coupling to an external bath. *J. Chem. Phys.* **81**, 3684–3690 (1984).
104. Bussi, G., Donadio, D. & Parrinello, M. Canonical sampling through velocity rescaling. *J. Chem. Phys.* **126**, 014101 (2007).
105. Parrinello, M. & Rahman, A. Polymorphic transitions in single crystals: a new molecular dynamics method. *J. Appl. Phys.* **52**, 7182–7190 (1981).
106. Brehm, M. & Kirchner, B. TRAVIS-a free analyzer and visualizer for Monte Carlo and molecular dynamics trajectories. *J. Cheminform.* **4**, F1 (2011).
107. Brehm, M., Thomas, M., Gehrke, S. & Kirchner, B. TRAVIS—A free analyzer for trajectories from molecular simulation. *J. Chem. Phys.* **152**, 164105 (2020).
108. Bannwarth, C., Ehlert, S. & Grimme, S. GFN2-xTB—An accurate and broadly parametrized self-consistent tight-binding quantum chemical method with multipole electrostatics and density-dependent dispersion contributions. *J. Chem. Theory Comput.* **15**, 1652–1671 (2019).
109. Neese, F. The ORCA program system. *Wiley Interdiscip. Rev. Comput Mol. Sci.* **2**, 73–78 (2012).
110. Roemelt, M., Maganas, D., DeBeer, S. & Neese, F. A combined DFT and restricted open-shell configuration interaction method including spin-orbit coupling: application to transition metal L-edge X-ray absorption spectroscopy. *J. Chem. Phys.* **138**, 204101 (2013).

111. Maganas, D. et al. First principles calculations of the structure and V L-edge X-ray absorption spectra of V_2O_5 using local pair natural orbital coupled cluster theory and spin–orbit coupled configuration interaction approaches. *Phys. Chem. Chem. Phys.* **15**, 7260–7276 (2013).
112. Axel, D. B. Density-functional thermochemistry. III. The role of exact exchange. *J. Chem. Phys.* **98**, 5648–5652 (1993).
113. Lee, C., Yang, W. & Parr, R. G. Development of the Colle–Salvetti correlation-energy formula into a functional of the electron density. *Phys. Rev. B* **37**, 785 (1988).
114. Schäfer, A., Horn, H. & Ahlrichs, R. Fully optimized contracted Gaussian basis sets for atoms Li to Kr. *J. Chem. Phys.* **97**, 2571–2577 (1992).
115. Weigend, F. & Ahlrichs, R. Balanced basis sets of split valence, triple zeta valence and quadruple zeta valence quality for H to Rn: design and assessment of accuracy. *Phys. Chem. Chem. Phys.* **7**, 3297–3305 (2005).
116. Kendall, R. A. & Früchtl, H. A. The impact of the resolution of the identity approximate integral method on modern ab initio algorithm development. *Theor. Chem. Acc.* **97**, 158–163 (1997).
117. Feyereisen, M., Fitzgerald, G. & Komornicki, A. Use of approximate integrals in ab initio theory. An application in MP2 energy calculations. *Chem. Phys. Lett.* **208**, 359–363 (1993).
118. Pantazis, D. A., Chen, X.-Y., Landis, C. R. & Neese, F. All-electron scalar relativistic basis sets for third-row transition metal atoms. *J. Chem. Theory Comput.* **4**, 908–919 (2008).

Acknowledgements

We acknowledge the advice on the manuscript from B. Dunn at the University of California, Los Angeles, and technical support from the Maryland NanoCenter. STXM was performed at the Canadian Light Source, a national research facility of the University of Saskatchewan. We thank the computational resources provided on Bebop, a high-performance computing cluster operated by the Laboratory Computing Resource Center at Argonne National Laboratory. This work was supported by the US Department of Energy (DOE: Grant No. DE-EE0008856 to C.W.; and Grant No. DE-AC05-76RL01830 to C.W.) and DOE, Office of Energy Efficiency and Renewable Energy (Grant No. DE-EE0009183 to C.W.). The XAS test was supported by DOE, Battery500 Consortium (Grant No. DE-SC0012704 to S.T., X.Y. and E.H.) and DOE, Office of Science User Facilities (Grant No. DE-SC0012704 to Brookhaven National Laboratory). We also thank the Analytical NMR Service & Research Center at the University of Maryland, College Park, for using 600 MHz solution and 500 MHz solid-state NMR spectrometers (supported by the National Science Foundation under Grant No. NSF-1726058).

Author contributions

W.Z. and C.W. proposed the research. W.Z. conceived the idea, performed the electrochemical, SEM and TEM experiments, and wrote the manuscript. V.K. and N.K.D. performed the molecular dynamics simulations and DFT calculations. S.L. helped with the electrochemical experiments and the SEM. P.B. helped with the FTIR. J.Z. and J.W. performed the STXM. S.T., X.Y. and E.H. performed the XAS. Z.W. helped with the analysis of the calculation results. J.X., H.W. and X.Z. helped with editing the manuscript. H.Y. performed the Instron mechanical test. B.L. and A.L. performed the XPS and analysed the results. F.C. performed the NMR spectroscopy. S.R. drew the schematic, edited the manuscript and supervised the analysis of the polymer properties. A.N. supervised the simulations and calculations, and C.W. supervised the study and the manuscript writing. All authors discussed the results.

Competing interests

The authors declare no competing interests.

Additional information

Supplementary information The online version contains supplementary material available at https://doi.org/10.1038/s41560-023-01443-0.

Correspondence and requests for materials should be addressed to Srinivasa R. Raghavan, Anh T. Ngo or Chunsheng Wang.

Peer review information *Nature Energy* thanks Grazia Accardo, Kan Hatakeyama-Sato and the other, anonymous, reviewer(s) for their contribution to the peer review of this work.